Article

Investigations of the Effect of H$_2$ in CO Oxidation over Ceria Catalysts

Arantxa Davó-Quiñonero [1,2,*], Sergio López-Rodríguez [2], Cristian Chaparro-Garnica [2], Iris Martín-García [3], Esther Bailón-García [2], Dolores Lozano-Castelló [2], Agustín Bueno-López [2] and Max García-Melchor [1,*]

[1] School of Chemistry, CRANN and AMBER Research Centres, Trinity College Dublin, College Green, Dublin 2 Dublin, Ireland

[2] Inorganic Chemistry Department, University of Alicante, Carretera San Vicente del Raspeig s/n, E-03080 Alicante, Spain; sergio.lopez@ua.es (S.L.-R.); cristian.chaparro@ua.es (C.C.-G.); estherbg@ugr.es (E.B.-G.); d.lozano@ua.es (D.L.-C.); agus@ua.es (A.B.-L.)

[3] Organic Chemistry Department, University of Alicante, Carretera San Vicente del Raspeig s/n, E-03080 Alicante, Spain; iris.martin@ua.es

[*] Correspondence: arantxa.davo@tcd.ie (A.D.-Q.); garciamm@tcd.ie (M.G.-M.); Tel.: +353-83-393-0023 (A.D.-Q.); +353-1-896-8485 (M.G.-M.)

Abstract: The preferential CO oxidation (so-called CO-PROX) is the selective CO oxidation amid H$_2$-rich atmospheres, a process where ceria-based materials are consolidated catalysts. This article aims to disentangle the potential CO–H$_2$ synergism under CO-PROX conditions on the low-index ceria surfaces (111), (110) and (100). Polycrystalline ceria, nanorods and ceria nanocubes were prepared to assess the physicochemical features of the targeted surfaces. Diffuse reflectance infrared Fourier-transformed spectroscopy (DRIFTS) shows that ceria surfaces are strongly carbonated even at room temperature by the effect of CO, with their depletion related to the CO oxidation onset. Conversely, formate species formed upon OH + CO interaction appear at temperatures around 60 °C and remain adsorbed regardless the reaction degree, indicating that these species do not take part in the CO oxidation. Density functional theory calculations (DFT) reveal that ceria facets exhibit high OH coverages all along the CO-PROX reaction, whilst CO is only chemisorbed on the (110) termination. A CO oxidation mechanism that explains the early formation of carbonates on ceria and the effect of the OH coverage in the overall catalytic cycle is proposed. In short, hydroxyl groups induce surface defects on ceria that increase the CO$_x$–catalyst interaction, revealed by the CO adsorption energies and the stabilization of intermediates and readsorbed products. In addition, high OH coverages are shown to facilitate the hydrogen transfer to form less stable HCO$_x$ products, which, in the case of the (110) and (100), is key to prevent surface poisoning. Altogether, this work sheds light on the yet unclear CO–H$_2$ interactions on ceria surfaces during CO-PROX reaction, providing valuable insights to guide the design of more efficient reactors and catalysts for this process.

Keywords: nano-shaped ceria; CO oxidation; CO-PROX; DFT calculations; reaction mechanism; DRIFTS; coverage effects

1. Introduction

Ceria-based materials have been extensively used as CO oxidation catalysts due to their unique redox features [1–3]. A particular niche of this application is the preferential CO oxidation (CO-PROX), which is the preferred catalytic strategy towards the removal of CO impurities from H$_2$ reformate streams [4,5]. The CO clean-up in these streams is crucial for the deployment of H$_2$-based fuel cell technologies, which currently rely on strongly CO-sensitive Pt electrodes [6]. Broadly speaking, CO-PROX consists in the selective oxidation of CO in a highly H$_2$-rich atmosphere. Besides good selectivity, this process requires a high CO conversion up to the remarkably low ppmv CO tolerance limit of Pt-based electrodes [7,8]. Furthermore, this should be achieved within a low temperature range

(ca. < 200 °C) and in the presence of $CO_2 + H_2O$ inhibitors. Therefore, the design of suitable active and durable CO-PROX catalysts is a challenge that has been partially addressed over years of fundamental and applied research. Among the state-of-the-art CO-PROX catalysts, CuO/CeO_2 materials have been consolidated due to their near-optimal catalytic outputs with admirable robustness, cyclability, resistance to CO_2 and H_2O inhibition and low cost [9].

CuO/CeO_2 systems are intrinsically complex materials wherein interfacial interactions of a synergistic redox nature occur, giving rise to unique catalytic features. It is well-reported that the improved reducibility of the catalyst by the labile Cu^{2+}/Cu^{+}-Ce^{4+}/Ce^{3+} redox interplay facilitates the formation of surface Cu^{+} species, pinpointed as the CO adsorption and oxidation sites [10–12]. On the other hand, since Cu^0 species are known to boost the undesired H_2 oxidation, CO selectivity is determined by the oxidation state of copper particles, which varies throughout the CO-PROX reaction [13]. In turn, tuning the redox features of the CuO/CeO_2 material has proven to have a direct impact on CO-PROX catalytic performance [14–16].

As an inherent characteristic of CO-PROX, CO selectivity drops with temperature, and the steepness of the fall mainly depends on the difference between the CO and H_2 oxidation reaction onsets [17]. Interestingly, although there are comprehensive reports addressing the competitive nature between CO and H_2 oxidation reactions on CuO/CeO_2, the underlying interaction of hydrogen with CO oxidation is still an unresolved question [11,18–20]. Some studies have reported that CO inhibits H_2 oxidation [11,18], while CO oxidation is favored by the presence of H_2 [21,22]. To date, different interpretations of this kinetic interplay have been proposed based on the CO-PROX selectivity dependence on the relative CO/H_2 surface coverages rather than on the O_2 partial pressure [18,23–25]. One hypothesis is that hydrogen hampers CO adsorption while promoting CO_2 desorption [26]. Polster et al. [11] reported that surface hydroxylation may displace CO from the adsorption sites on a CuO/CeO_2 catalyst, although CO binding was strengthened by surface hydration. A complementary hypothesis considers the chemical CO–H_2 interaction as a source of formates [27,28], which are deemed to promote CO oxidation on Pt/Al_2O_3, although accumulation of adsorbate species can lead to catalyst deactivation [29]. Other hypotheses consider that OH groups could facilitate the formation of partially hydrogenated intermediates (e.g., bicarbonates) with an overall beneficial effect on the reaction kinetics due to their faster desorption rate [30,31]. Altogether, these studies indicate that the nature of the CO–H_2 interaction depends on the specific properties of the studied catalyst, which dictate the prevalence of the reaction mechanism.

In ceria-based catalysts, spectroscopic studies have evidenced the formation of carbonaceous species such as carbonates and bicarbonates at room temperature under CO-PROX mixtures [32,33], while formates typically appear at temperatures beyond 100 °C [28]. Carbonates and bicarbonates are retained products of CO oxidation, and their presence below the CO oxidation onset along with the formation of Cu^{+} carbonyls indicate the occurrence of a low-temperature CO oxidation. Previously, we reported that the rate of CO oxidation might be controlled by product desorption in a low-temperature regime when CO_2 is accumulated on the ceria surface as strongly bound carbonate groups. The results showed that the formation of less stable bicarbonate intermediates resulted in a positive effect on CO oxidation kinetics [30]. Hence, the presence of H_2 promotes CO oxidation prior to the hydrogen oxidation reaction onset point, beyond which OH groups are released in the form of water by means of lattice oxygen abstraction in a process that competes with CO oxidation. Beyond a critical low temperature, the nature of the carbonaceous intermediates formed during CO oxidation becomes irrelevant as product desorption is relatively fast.

To the best of our knowledge, a theoretical description of the CO-PROX reaction mechanism within the CO selective regime has not been reported to date. In such low-temperature operating conditions, the catalyst coverage can determine the reaction kinetics by forming strongly bound intermediates, reaction products, or mere spectators of different

nature. Given that carbonaceous species are known to be mainly accumulated on the ceria support, in this article we report a thorough investigation of the adsorption and evolution of carbonates, formates and bicarbonates on the low-index CeO_2(111), CeO_2(110) and CeO_2(100) surfaces by means of periodic density functional theory (DFT) calculations. The reaction mechanism under experimental CO-PROX conditions has been mapped out, including the transition states (TS) involved in the key reaction steps. In addition, the theoretical studies of the CO–H_2 interaction on the various ceria surfaces have been complemented with experimental characterization of shape-engineered ceria samples representative of the modelled terminations. CO-PROX operando diffuse reflectance infrared Fourier-transformed spectroscopy (DRIFTS) experiments were conducted to identify the formation and evolution of adsorbed species. The textural, redox and crystalline features of polycrystalline ceria, nano-cubes and nano-rods were evaluated in order to understand the facet-dependent behavior under the CO-PROX reaction mixtures. Altogether, this work presents a dual approach to the study of the CO–H_2 interaction on ceria-based catalysts. The insights derived from this work may contribute to deepen the fundamental understanding of the role of the support in metal-loaded ceria catalysts of great technological and commercial interest.

2. Results

2.1. Characterization of Ceria Surfaces

2.1.1. Physicochemical Features of Nano-Shaped Ceria Samples

Polycrystalline ceria, nano-cubes and nano-rods display distinct characteristic structural features that determine their crystallinity and textural properties. While polycrystalline ceria is the mere product of calcination of cerium precursors, nano-shaped materials were prepared through hydrothermal methods as described in Section 4.1. Figure 1 compiles Raman spectroscopy (a), TEM (b), and N_2 physisorption analyses (c) of the synthesized ceria samples. Raman spectra (Figure 1a) provides information of the crystalline structure with sufficient sensitivity to reveal any changes in the lattice parameter and crystalline disruptions. In general, Raman spectra of CeO_2 exhibit a distinctive vibrational mode at ca. 462 cm^{-1} ascribed to the oxygen in the fluorite lattice (F_{2g}) [34]. At ca. 590 cm^{-1} is located the D band, traditionally assigned to the presence of lattice defects such as oxygen vacancies [35]. However, the overlap with second-order bulk vibrational modes (i.e., A_{1g}, F_{2g} and E_g) brings inaccuracy to the assumption of a direct relation between defects and the D band contribution [36]. Other minor bands at ca. 250 and 405 cm^{-1} can be attributed to the vibration of surface Ce-O bonds [37], while the weak band appearing at 1170 cm^{-1} is the second-order Raman mode 2LO. Table 1 displays the position of the F_{2g} band maxima and the D/F_{2g} band ratio, calculated for each sample. Ceria nanocubes exhibit a blue-shifted F_{2g} band maxima by 2.0 cm^{-1}, which evidences significant differences in the particle sizes compared to the other counterparts [38].

Table 1. Physicochemical characterization results for the nano-shaped ceria materials extracted from Raman spectroscopy, N_2 physisorption isotherms, X-ray diffraction and X-ray photoelectron spectroscopy (XPS).

Material	F_{2g} (cm^{-1})	D/F_{2g} Band Ratio	S_{BET} (m^2/g)	V_{micro} (cc/g)	a (nm)	D (nm)	Surface Ce^{3+} (%)	O_{lab}/O_{lat} (%)
Polycrystalline	462.6	0.05	71	0.04	5.411	9.5	21	30
Nanocubes	464.6	0.05	30	0.00	5.414	22.5	26	35
Nanorods	462.6	0.06	93	0.06	5.411	9.0	21	19

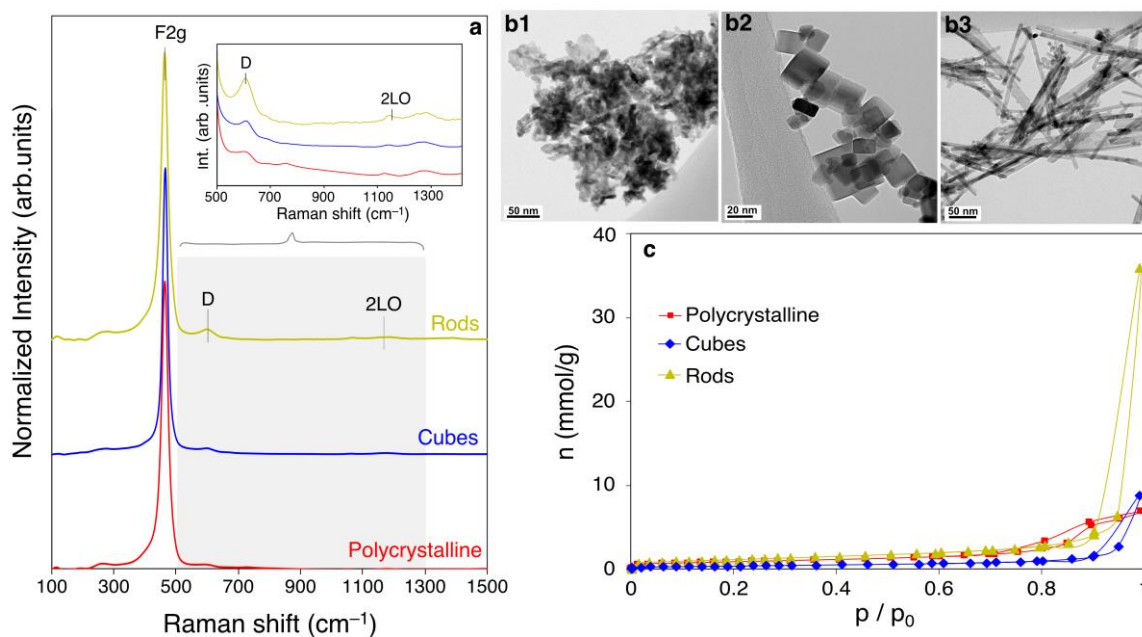**Figure 1.** (**a**) Raman spectra of the prepared ceria catalysts with zoomed 500–1300 cm^{-1} range inset; (**b**) TEM images of polycrystalline ceria (**b1**), nano cubes (**b2**) and nano rods (**b3**); (**c**) N$_2$ physisorption isotherms recorded at −196 °C for the different ceria samples.

Data extracted from X-ray diffractograms (Figure S1) reveal that lattice parameters (a) are consistent with the reported for ceria [39]. However, nanocubes exhibit a greater crystallite size (D, Scherrer equation) of i.e., 22.5 nm in contrast to the ca. 9 nm determined for polycrystalline ceria and nanorods, as seen in Table 1. On the other hand, D/F$_{2g}$ ratios suggest that nanorods present a higher concentration of oxygen vacancies, in line with previous observations [40,41], although the recorded XPS spectra (Figure S2) rule out the greater intrinsic reduction of the ceria surface in the rod-like sample. The percentage of reduced Ce ions (3+) calculated from the corresponding contributions in the Ce 3d XPS region (Figure S2b) [42] is shown in Table 1, besides the labile to lattice O ratio (O$_{lab}$/O$_{lat}$) determined from the O 1s region (Figure S2c). According to these parameters, cubes exhibit a slightly more reduced surface, which is consistent with the blue shift observed in the F$_{2g}$ Raman band.

Transmission electron microscopy (TEM) (Figure 1b) provides visual confirmation of the targeted crystal morphology in each case. Namely, ceria polycrystalline (Figure 1b1) are constituted by irregular particles in size and shape, nanocubes (Figure 1b2) display a cubic-like crystals, while nanorods (Figure 1b3) exhibit a characteristic nanofibrillar array. In the case of the polycrystalline sample, it is composed by a variety of polyhedral-shaped particles with predominance of the low energy {111} planes. On the contrary, it has been extensively reported in literature that nanocubes expose six {100} facets, while corners and edges are composed by the {111} and {110} terminations. On the other hand, nanorods are built upon the crystal growth along the [110] direction, dominated eventually by a mixture of {110} and {100} surface planes [43]. The characteristic lattice fringes assessed by TEM characterization (Figure S3) confirm the abundance of the representative terminations in the prepared set of materials [44].

N$_2$ physisorption isotherms (Figure 1c) display typical type IV isotherms characteristic of micro/mesoporous materials [45]. However, whilst polycrystalline ceria exhibits a type H2(b) hysteresis loop, nanocubes and nanorods show a type H3. H2(b)-type hysteresis is a sign of a broad pore size distribution, whereas type H3 is characteristic of non-rigid plate-like aggregates [46]. The calculated B.E.T. surface area and total micropore volume are presented in Table 1, revealing that the porosity increases according to the following trend: nanocubes << polycrystalline < nanorods. The lower porosity assessed for cubes

agrees with the bigger crystallite size of the cubic-like particles. On the contrary, rods display an enlarged porosity compared to the polycrystalline sample mainly due to the additional presence of macropores, as evidenced by the sharp increase at the maximum relative pressure. The enriched porosity in the meso/macro range can be related to the lower packing density of rod-like particles, leading to a broader interparticle space [47].

2.1.2. Computational Simulation of Low-Index Ceria Surfaces

The low-index CeO_2 surfaces (111), (110) and (100), representative of polycrystalline ceria, nanorods and nanocubes, respectively, have been modelled by means of periodic DFT calculations (see Section 4.4 for details). The constructed surface slabs used in the calculations are illustrated in Figure 2a. In short, CeO_2(111) is an O-terminated non-polar O-Ce-O-O-Ce-O structure with p(2 × 2) periodicity presenting four coordinatively unsaturated O atoms on the surface. On the other hand, the (110) slab is a Ce–O terminated surface wherein neutrality is kept within each atomic layer. The periodicity of this slab was set to p(2 × 1), resulting in eight coordinatively unsaturated O atoms on surface. Finally, the CeO_2(100) slab consists of alternate Ce-O-Ce-O arrays, which results in a net polar character with a dipole moment oriented along the z axis. To avoid any potential dipole effects in our DFT calculations, the (100) slab was reconstructed by moving half of the surface O atoms to the bottom layer, resulting in a surface exposing four unsaturated O atoms, as in the case of CeO_2(111).
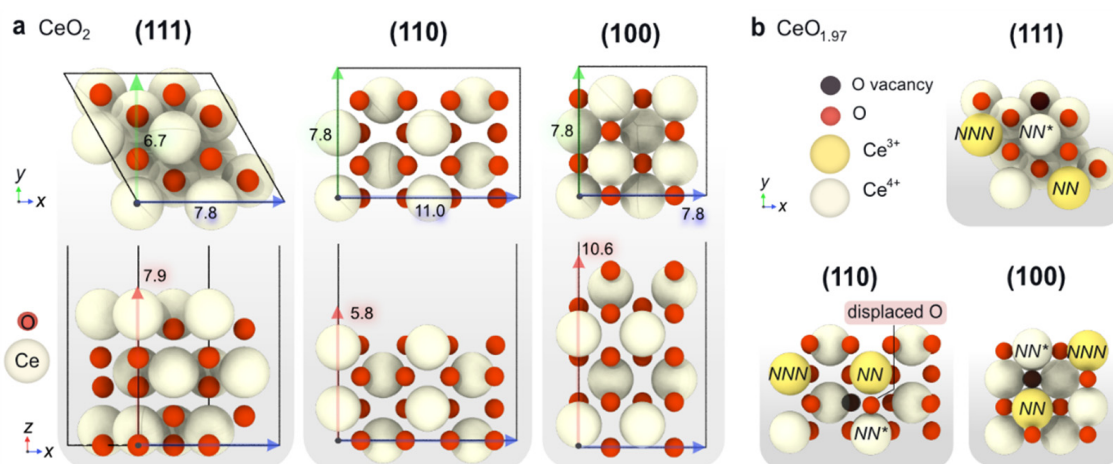

Figure 2. (**a**) Top (above) and side (below) views of the DFT-modeled stoichiometric surface slabs CeO_2 (111), CeO_2 (100) and CeO_2 (110). The slab dimensions are also given (in Å). (**b**) Top view of the non-stoichiometric slabs featuring one O surface vacancy with the polaron localized in the most stable configuration. *NN* and *NNN* denote the nearest neighbor and next-nearest neighbor positions with respect to the O vacancy, respectively.

As depicted in Figure 2, the modeled slabs display different atom packing density, which gives rise to different surface energies, as shown in Table 2. The calculated surface energies follow the trend (111) > (110) > (100), which is in good agreement with previous theoretical works [43,48]. Since ceria-based catalysts are known to participate in oxidation processes through their labile lattice oxygens [49,50], the oxygen vacancy formation energy (E_{vac}) has been proposed as reaction descriptor [51–53]. However, Kropp and Mavrikakis [54] recently demonstrated a non-monotonic relationship between CO oxidation barriers and E_{vac} in reducible catalysts, given the variable nature of E_{vac} alongside the reaction conditions. In any case, E_{vac} values can serve as good indicators of the intrinsic relative readiness of the surface to provide active oxygen, which is eventually refilled by O_2 gas molecules.

Table 2. Summary of the DFT results of the modelling of the different ceria slabs. From left to right: surface energy (γ); O vacancy formation energy (E_{vac}); electron localization upon O vacancy formation (e^- distr.); Energies of O_2 adsorbed species (*O–O) on the O vacancy site referenced to the clean sur-face (ΔE_{O2}); and the corresponding type, i.e., O_2^- (superoxide) or O_2^{2-} (peroxide).

Surface	Formula	γ (eV/Å^2)	E_{vac} (eV/O Atom)	e^- Distr.	E_{ads} O_2 (eV)	Type *O_2
$CeO_2(111)$	$Ce_{12}O_{24}$	0.044	2.22	*NN/NNN*	0.79	O_2^-
			2.71	*NN/NN*	0.36	O_2^{2-}
$CeO_2(110)$	$Ce_{16}O_{32}$	0.075	1.32	*NN/NNN*	0.72	O_2^-
			1.80	*NN/NN*	0.17	O_2^{2-}
$CeO_2(100)$	$Ce_{16}O_{32}$	0.113	1.68	*NN/NNN*	0.26	O_2^-
			1.76	*NN/NN*	−0.34	O_2^{2-}

Note: (*) stands for the adsorption site.

Table 2 shows the computed E_{vac} for each surface slab, which strongly depends on the electron localization upon O vacancy formation [55]. In particular, the abstraction of an O^{2-} anion from the lattice results in a charge imbalance of +2, which is restored by the reduction of two Ce^{4+} cations to Ce^{3+}. In the CeO_2 slabs, the nearest neighbor Ce ions to the O vacancies are labelled as *NN*, while *NNN* denotes the next-nearest neighbors. Our calculations indicate that the most stable rearrangement is *NN/NNN* regardless of the surface facet, leading to the following trend in the oxygen vacancy formation energy: (111) > (100) > (110). The optimized non-stoichiometric slabs after the formation of one oxygen vacancy are shown in Figure 2b. Noticeably, the *NN/NNN* configuration for the non-stoichiometric (110) surface leads to the lowest energy, i.e., 1.32 eV, which corresponds to 0.17 eV per surface O atom. Conversely, the (100) termination has associated a larger oxygen vacancy formation energy, despite exhibiting a lower atomic density. Regarding this, while the ongoing ionic relaxations upon O-vacancy formation in (111) and (100) are moderate, in (110), the neighboring surface O is significantly displaced towards an equidistant position between the original *NN* and *NN* Ce^{4+} cations. This higher relaxation in the (110) surface results in a reduced E_{vac}.

Since the oxygen vacancy must be refilled with an incoming O_2 to complete the catalytic cycle, we investigated the interaction between the ceria surfaces and the O_2 molecule. Table 2 compiles the lowest O_2 adsorption energies (E_{ads}) for the non-stoichiometric slabs containing one O-vacancy in their most favored electronic distribution. Among the reactive oxygen species that can be formed upon O_2 adsorption on the oxygen vacancy, peroxides (O_2^{2-}) and superoxides (O_2^-) must be highlighted. Superoxides and peroxides exhibit different spin states (i.e., triplet and singlet, respectively) and the latter are generally lower in energy [56]. It is assumed that O_2 adsorption and O lattice restitution proceeds via the following steps: O_2 (g)–O_2^-–O_2^{2-}–2 O^{2-}, wherein superoxides naturally evolve to peroxides. Previous theoretical studies [57–59] have also reported in detail the healing of oxygen vacancies in different ceria surfaces and our results are in close agreement, though the computed energies may differ slightly due to the particularities of the models employed. O_2 adsorption on the O vacancy leads to a tilted *O-O molecule with elongated bond distances of ca. 1.35 and 1.44 Å for superoxides and peroxides, respectively. In the case of peroxides, the vacancy site is healed by one of the O atoms, while the other can diffuse on the surface to refill a second O vacancy present in the neighboring sites. Huang et al. [57] reported that the energy barrier for the diffusion of an O adatom is ca. 1.4 eV for (111) and 1.70 eV for (110), which suggests that peroxides may be present as reactive adsorbates at low temperatures. In these conditions, the second O could remain loosely bound to the just refilled O vacancy and be available to react with new incoming reactant species, such as CO or H_2. Recently, Ziemba et al. [60] have reported a study of the interaction of O_2 with reduced ceria surfaces, demonstrating a close correlation between the outcomes from state-of-the-art spectroscopy techniques and theory. Herein, the participation of

these reactive oxygen species in the CO-PROX mechanism has been carefully investigated (vide infra).

2.2. CO Oxidation Operando DRIFTS Experiments

The catalytic performance of undoped CeO_2 with different morphologies in CO oxidation and other processes has been previously reported [61–64]. In short, these studies confirm that tuning the morphology of CeO_2 to increase specific surface area and selectively expose the (110) facet has a critical effect on CO oxidation activity. In this work, polycrystalline ceria samples expose mostly (111) facets, while (110) surfaces are also abundant according to TEM characterization (Figure S3). Hence, this material has interesting features in terms of simplicity, stability and reactivity, and for this reason, we will focus on this sample. In particular, in this section we describe our investigations on the CO oxidation mechanism by means of DRIFT spectroscopy experiments in two different set of conditions: (a) in presence of an excess of H_2 (CO-PROX); (b) in a H_2-free atmosphere (CO-TOX).

Figure 3a,b display the characteristic vibration modes of adsorbates found on the CeO_2 catalytic surface during CO oxidation in the presence and absence of an excess of H_2 (i.e., CO-PROX and CO-TOX conditions, respectively). From left to right, the 4000–2500 cm^{-1} region contains the fingerprint vibrational O-H and C-H stretching modes. Isolated hydroxyl groups are located in the 3700–3670 cm^{-1} range as narrow bands, and the coordination of OH groups to the surface determines the frequency of the O-H stretching mode. In particular, monocoordinated OH species show higher wavenumber compared to bi- and tricoordinated OH groups. On the other hand, the position of the bands is also known to be sensitive to surface Ce reduction, while increasing the temperature leads to the depletion of isolated OH groups during CO oxidation experiments, being assigned to Type II hydroxyls (bicoordinated) with center at 3670 cm^{-1} [65,66].

The presence of H_2 in the reaction stream additionally leads to the consumption of higher frequency OH groups (i.e., 3690 cm^{-1}), attributed to monocoordinated hydroxyls or OH on Ce^{3+} sites [67]. On the other hand, H-bonding between surface OH groups and H_2O molecules, a characteristic feature of high OH coverages, display a broad absorption band in the 3600–2800 cm^{-1} range. Both in presence and absence of H_2, polybonded surface OH moieties are depleted upon CO oxidation, though in the presence of H_2 a more dramatic effect is observed. As has been well reported, the interaction of ceria with H_2 mixtures leads to surface reduction by H_2 adsorption and H_2O release [68]. Under experimental conditions, in presence of inlet O_2, the removal of H_2O may also be due to the competing H_2 oxidation reaction.

C-H vibration modes are found in the 2700–2950 cm^{-1} range which can be attributed to formate species. Since formates are generated during CO oxidation independently of H_2 co-feeding, the intrinsically present OH groups must be involved. In particular, the characteristic frequency of C-H bond stretching [$\nu(CH)$] of formates is reported at 2845 cm^{-1}. Minor bands with centers at 2930 and 2730 cm^{-1} are also associated with formates, being ascribed to the combination of the C-H bending + the asymmetric OCO stretching [$\delta(CH)$ + $\nu(OCO)$] modes and the C-H bending overtone [$2\delta(CH)$]. Hence, regardless of the presence of H_2 in the reaction stream, formates are formed during CO oxidation on the ceria surface. Finally, minor evidence of formyl species (CHO) at incipient stages of CO oxidation is revealed by their characteristic $\nu(CH)$ band at 2790 cm^{-1}. Overall, our results show that CO oxidation involves the participation of OH groups via (i) inherently present OH species, and/or (ii) the dynamic H_2 dissociative adsorption. Further confirmation of formate (OCHO) species is found in the 1900–900 cm^{-1} range, as described below.
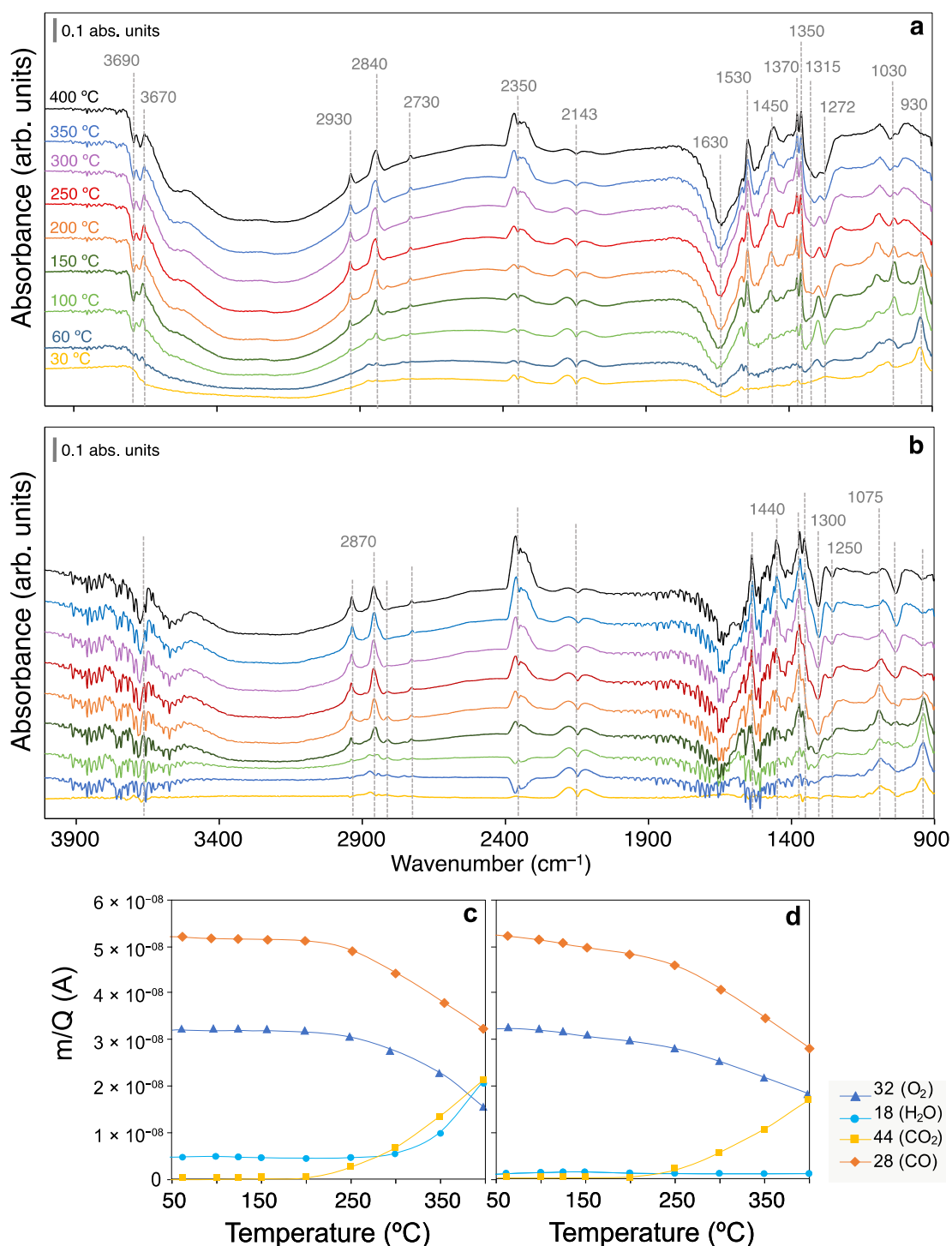
Figure 3. Operando DRIFT spectra recorded at different temperatures with the polycrystalline CeO_2 catalyst under (**a**) CO-PROX and (**b**) CO-TOX conditions. Below, evolution with temperature of the average outlet m/Q signals at steady conditions evolved from the DRIFTS reaction cell in (**c**) CO-PROX and (**d**) CO-TOX experiments.

The P and Q rotational branches of CO_2 and CO gases are located at ca. 2350 cm^{-1} and 2143 cm^{-1}, respectively. Note that the initial decrease in CO_2 band relates to the presence of residual CO_2 during the He-background measurement, released upon the in situ sample preconditioning in O_2. In the experimental conditions of the DRIFTS setup, the weak $Ce^{\delta+}$-CO carbonyl band was not discerned below the CO gas band in the presence or absence of H_2. Conversely, the interaction of ceria with CO leads to the formation of carbonate-like

species as revealed by the numerous bands in the 1600–1000 cm^{-1} region. Importantly, the co-presence of H_2 in the reaction stream has an apparent effect on the surface coverage, but not on the nature of the adsorbate species. Thus, carbonate and formates are found to be stabilized on ceria even at temperatures below the CO oxidation onset. This indicates that CO is prone to reduce the ceria surface via a low temperature adsorption (below 100 °C), and since CO-PROX conditions show an apparent higher coverage, the co-presence of H_2 enhances CO retention in the form of formates and carbonates. On the other hand, the negative evolution in the bands located at ca. 1630, 1420 and 1280 cm^{-1} reveals the consumption of bicarbonate groups (HCO$_3{}^-$) during the CO oxidation. This observation suggests that CO evolves to carbonate-like species and formates, whilst the advance of the reaction reduces the coverage of bicarbonates.

To shed light on the above experimental results, we carried out a computational investigation of the adsorption modes of CO on the various ceria surfaces under representative conditions of CO-PROX and CO-TOX experiments.

2.3. DFT Simulation of CO-PROX Reaction in Ceria Catalysts

2.3.1. Surface Coverage Studies in CO-PROX Conditions

Firstly, the resting state of each of the ceria surfaces under relevant CO-PROX conditions was determined. Upon the dissociative adsorption of H_2, two OH groups are formed [69] leading to the one-electron reduction of two Ce^{4+} surface sites to Ce^{3+}. Since theoretical calculations have demonstrated that H_2 dissociation on ceria is thermodynamically driven at relatively low temperatures [70,71], the H coverage was assessed herein by calculating the energies of ceria surfaces covered with different concentrations of OH groups. The coverages explored and their corresponding relative Gibbs energies in the temperature range of 25–350 °C are represented in Figure 4a–c. As can be observed, throughout the temperature window of interest in CO-PROX (i.e., 25–200 °C), ceria surfaces are predicted to be covered by H in the form of OH groups. In particular, the four surface O atoms in CeO_2(111) and CeO_2(100) are fully hydrogenated (4 OH), while the eight surface oxygens in CeO_2(110) are terminated with 4 OHs and 2 CO moieties strongly stabilized as carbonates (see below).

With regards to CO, the Gibbs adsorption energies of this species on the clean (111) and (100) surfaces are relatively weak (i.e., −0.18 and −0.33 eV, respectively) compared to hydrogen. On the contrary, CO binds very strongly on the (110) surface as a carbonate-like species with an energy of –3.66 eV, in good agreement with the literature [72–75], leading to the reduction of two neighboring Ce^{4+} cations.

Figure 5 shows the most stable configurations of the adsorbates found in CO oxidation conditions on each stoichiometric ceria surface. Since the coverage analysis reveals that OHs populate the ceria surfaces in the presence of H_2, the Gibbs adsorption energies of *CO$_x$ adsorbates at different temperatures and OH coverages were computed, and are presented in Tables S1–S3. Interestingly, the binding modes of *CO$_x$ species remain unaltered in the presence of OH coverage despite the local Ce reduction induced by H_2 dissociation leads to stronger *CO$_x$–ceria interactions. Ceria surfaces may present two types of Lewis basic sites for CO$_x$ adsorption, namely surface oxygens and hydroxyls [76]. Whilst OHs are deemed as weaker base centers [77], their presence on the surface increases the Lewis basicity of surface oxygens due to the coexistence of reduced Ce^{3+} cations. Thus, CO_2 adsorption on the hydroxylated surfaces gives rise to bicarbonates (O*COOH), while CO_2 adsorption on O sites leads to carbonates (O*COO). On the other hand, the adsorption of CO on OH-covered ceria surfaces can lead to formates (O*CHO), which are very stable.
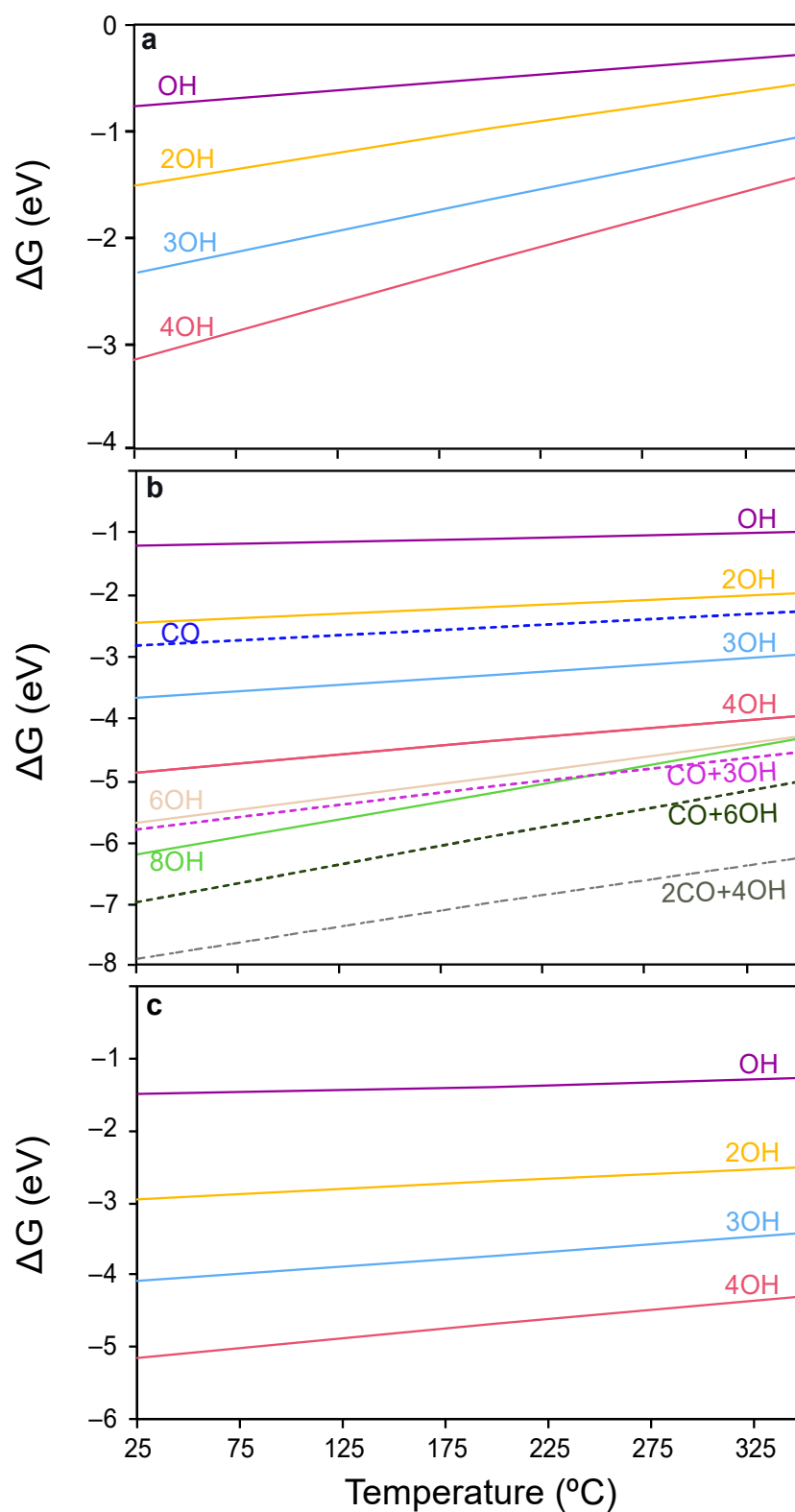
Figure 4. Coverage analysis on the ceria surfaces (**a**) (111), (**b**) (110) and (**c**) (100). Solid lines denote OH coverages, while dotted lines represent mixed coverages of OH and CO groups.
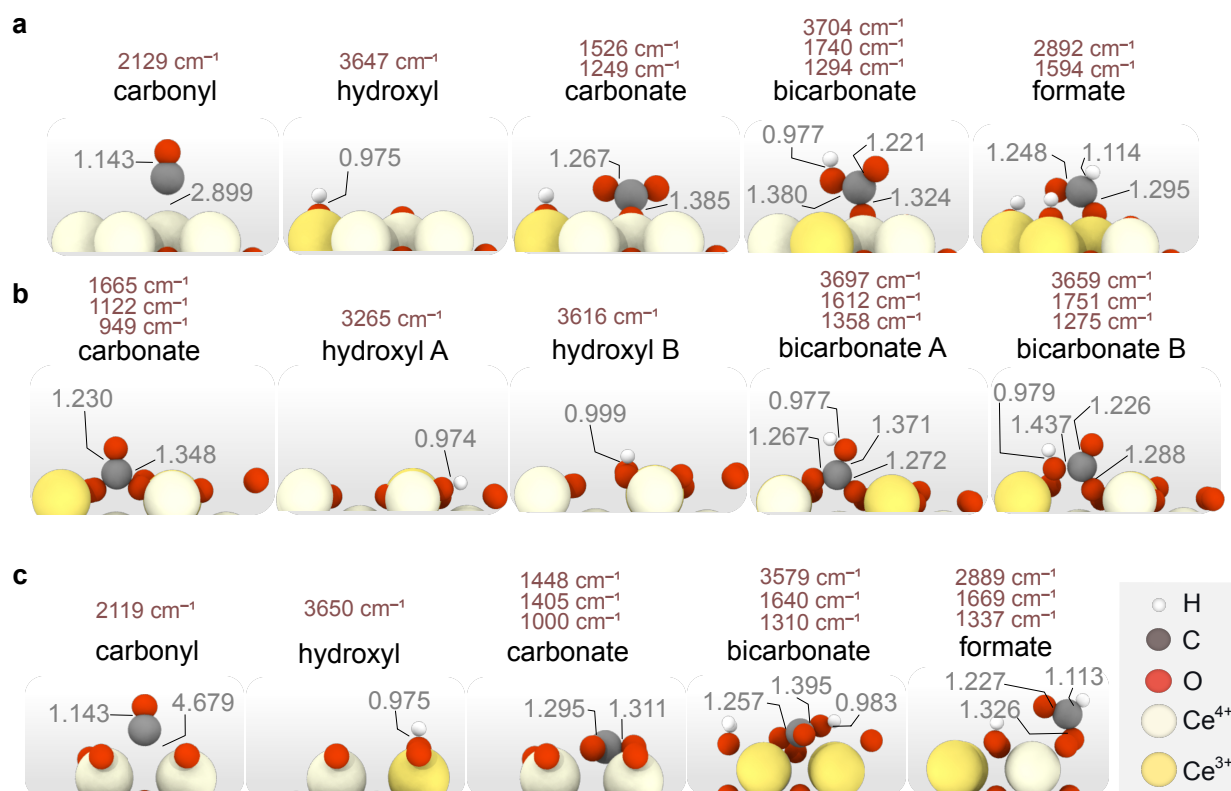
Figure 5. Representation of the most energetically favorable adsorption modes for CO, CO_2 and H_2 on stoichiometric (**a**) $CeO_2(111)$, (**b**) $CeO_2(110)$, (**c**) $CeO_2(100)$. Calculated vibrational frequencies (in cm^{-1}) and relevant distances (in Å) are also shown.

DFT calculations also reveal that the type of surface carbonate species varies with the surface termination. In particular, carbonates formed upon CO_2 adsorption on $CeO_2(111)$ display a monodentate mode, while on $CeO_2(100)$ they adopt a multidentate geometry with a much lower relative energy (i.e., −1.96 vs. −0.46 eV). Similarly, CO_2 adsorption on the clean (110) surface results in a monodentate carbonate with a relative energy of −1.31 eV (not shown in Figure 5 since the carbonate formed upon CO adsorption has a remarkably greater stability).

As regards to CO, this species merely physisorbs on top of Ce in $CeO_2(111)$, while it forms a bridged Ce-CO carbonyl on $CeO_2(100)$, and a strongly bound bidentate carbonate on $CeO_2(110)$. In addition, the most stable bicarbonate binding modes vary on the different surfaces, being monodentate in (111), bidentate in (110) and multidentate in (100). Finally, from the calculated CO_2 adsorption energies on the clean surfaces, we can conclude that the strength of the Lewis basic sites increases according to the trend (111) < (110) < (100), in agreement with the literature [77]. Our calculations also indicate that OH coverages hinder CO_2 adsorption as carbonates on the ceria surfaces. An exception, however, is the CO adsorption on (110) since the formation of a carbonate species provides a larger stabilization than the OH coverage, as observed in Figure 4b (4 OHs vs. CO + 3 OHs). Altogether, DFT calculations indicate that ceria surfaces will be hydroxylated under CO-PROX conditions and that no surface oxygens may be available. In the next section, the CO oxidation mechanism is studied on both the clean and OH-covered ceria surfaces representative of CO-TOX (H_2-free CO oxidation) and CO-PROX conditions. Since $CeO_2(100)$ is the least exposed surface in representative polycrystalline ceria samples, given it has the highest surface energy, our further reactivity studies placed more focus on the (111) and (110) facets.

2.3.2. CO Oxidation on CeO_2 in CO-PROX Atmosphere

To discern the potential catalytic effect of H_2 on CO oxidation, two scenarios are contemplated in the present study, namely a ceria clean surface and a hydroxylated surface.

- $CeO_2(111)$ clean surface

Figure 6 shows the lowest energy mechanism found for CO oxidation on the clean $CeO_2(111)$ surface.
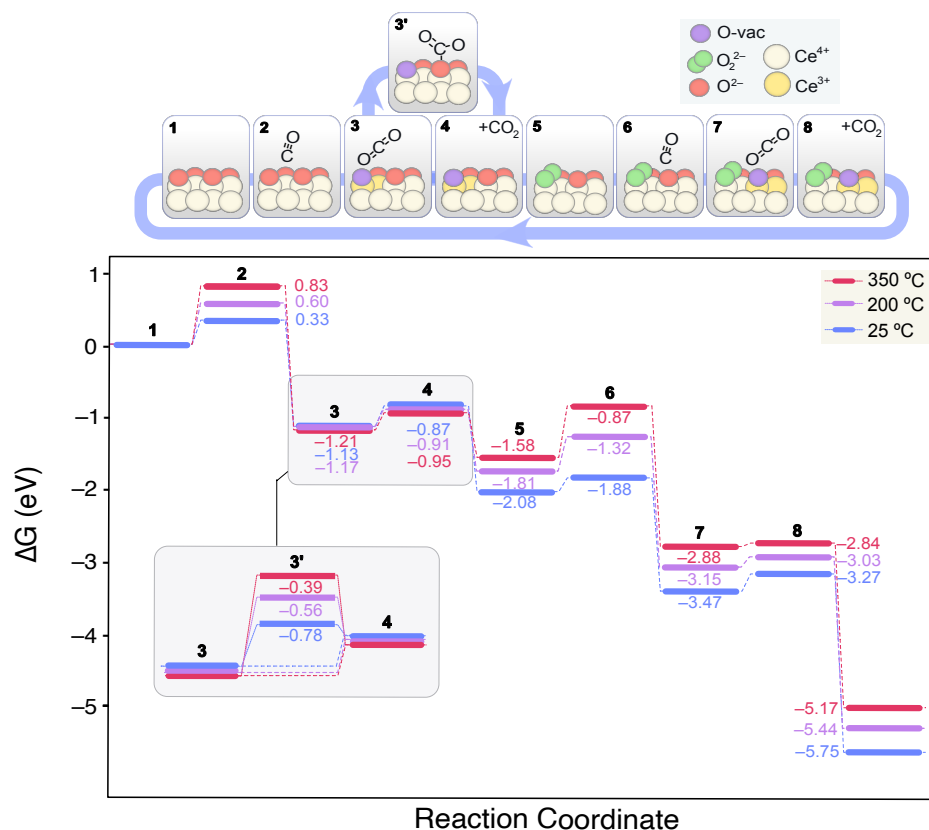

Figure 6. Calculated Gibbs energy diagram for the CO oxidation mechanism on a stoichiometric $CeO_2(111)$ clean surface at different experimental temperatures. The structures of the different reaction intermediates are depicted at the top of the diagram.

On the clean $CeO_2(111)$ surface, CO remains physisorbed at 2.899 Å from a surface Ce^{4+} ion (**2**). The CO Gibbs binding energy increases with temperature from 0.33 to 0.83 eV within the range of 25 to 350 °C. Next (**3**), CO diffuses from the top-Ce position to bind a surface O^{2-} leading to CO_2 and an oxygen vacancy (V^O). This process is exergonic by −1.46 eV (at 25 °C) given the increased stability of CO_2 with regards to CO. The resulting CO_2 is physisorbed on the boundaries of the recently formed V^O. Subsequently, it can be either directly desorbed to the gas phase (**4**) or chemisorbed on another surface O^{2-} giving rise to a carbonate CO_3^{2-} species (**3′**). Although at room temperature these processes might be in equilibrium, the release of CO_2 to the gas phase will prevail at higher temperatures. Next, the O_2 adsorption on the V^O leads to a peroxide (O_2^{2-}) intermediate (**5**), which restitutes the oxidized redox state of ceria, lowering the energy by −1.21 eV at 25 °C. From this state, a new CO molecule could interact with the surface as in (**2**). The CO binding energy on this surface (**6**), however, does not change when compared to that on the clean slab (**2**), and no interaction between *CO(ads) and $*O_2^{2-}$ (ads) was observed. On the contrary, as in (**3**), the interaction between the O^{2-}(lat) bound to CO leads to the release of $*CO_2$(ads) and the concomitant formation of a new V^O. Finally, the loosely bound O from the peroxide group migrates to the neighboring V^O and refills it recovering the original state and closing the catalytic cycle (**9**).

In this reaction scheme, the endergonic steps are essentially the weak CO adsorptions, whereas the overall process is thermodynamically very favored. In fact, the interaction is so weak that it is also claimed that CO oxidation may proceed via Eley–Rideal mechanism on ceria, involving a CO from the gas phase reacting with surface O [78]. This is corroborated by our CI-NEB results, where no transition state (TS) could be found for this process, but a V-bent structure with a partially formed C–O–O bond (see Figure S4).

- 2 OH-covered CeO_2(111) surface

Based on the coverage analysis presented in Figure 4a, the CeO_2(111) slab is fully hydroxylated under CO-PROX conditions, meaning that all surface oxygens are hydroxylated. However, in contrast to O^{2-} our results showed that CO is not capable to directly bind to OH. Herein, we opted to study a 2 OH-covered surface to model the ceria in the CO-PROX reaction so that O^{2-} sites are available for the reaction. Nevertheless, we modelled the reaction mechanism under different coverages to assess the best pathway and rule out a OH coverage dependence. According to this analysis, the presence of a third OH group systematically increases the stability of the CO_x intermediates on the surface, while the relative energy difference between steps is not significantly affected. Thus, although high OH coverages impede the CO-surface interaction by extensively blocking the active O^{2-}, the residual freely-exposed O^{2-} sides will display an enhanced basicity.

To deplete the stable OH groups on CeO_2(111), sufficient energy must be provided for these OH to recombine giving rise to H_2O and a V^O. Then, new available O^{2-} sites would be formed by the subsequent refilling by O_2 from the gas phase. The energy for OH recombination was calculated to be endergonic by 1.68 eV at 25 °C, and 1.30 eV at 200 °C (see Table S1). Thus, at temperatures above 200 °C it is expected that some of the hydroxyl groups recombine leading to oxygen vacancies and increasing lattice defects.

Figure 7 shows the lowest energy mechanism found for CO oxidation on the 2 OH-CeO_2(111) surface. In contrast to the clean, fully oxidized surface, CO can form a carboxylate ($*OCO^{2-}$) on the 2 OH-covered surface, a V-shaped CO_2 molecule with a O–C–O angle of 134.3° (structure 3 in Figure 7). The formation of carboxylates, also known as carbonites, is thermodynamically driven even at 25 °C by the adsorption of CO on a surface oxygen according to: CO(gas) + O^{2-}(lat) → CO_2^{2-}(ads). This process was modeled by means of CI-NEB calculations (see Figure S5), displaying two low energy transition states of 0.24 and 0.33 eV, structures corresponding to CO approaching and $C–O^{2-}$(lat) bond formation. Carboxylates have been found on pre-reduced ceria surfaces [79], and naturally lead to carbonates (CO_3^{2-}) either by further interaction with surface oxygen or with gaseous O_2. Carboxylates can also serve as precursors of formate species when neighboring OH groups are present (**3′**).

TS1 in Figure 7 refers to the formation of formate from carboxylate, which according to our calculations, requires an activation energy of ca. 1 eV. This low activation energy for formate formation, is consistent with these species being observed by DRIFTS at temperatures as low as 60 °C. In fact, formates are very stable species with relative Gibbs energies of −1.56, −2.22 and −3.02 eV at 350 °C when surrounded by one, two or three OH groups, respectively. Even at high OH coverages, formates are significantly stabilized as their evolution towards CO(ads) + *OH is very energy demanding, as recently showed in our mechanistic study of the CO_2 methanation reaction on ceria [80]. Hence, we predict formates to accumulate on ceria for a broad temperature window, as observed by DRIFTS. Even without H_2 in the reactant stream (CO-TOX conditions), formates are detected experimentally during CO oxidation around the same temperatures than in CO-PROX conditions.
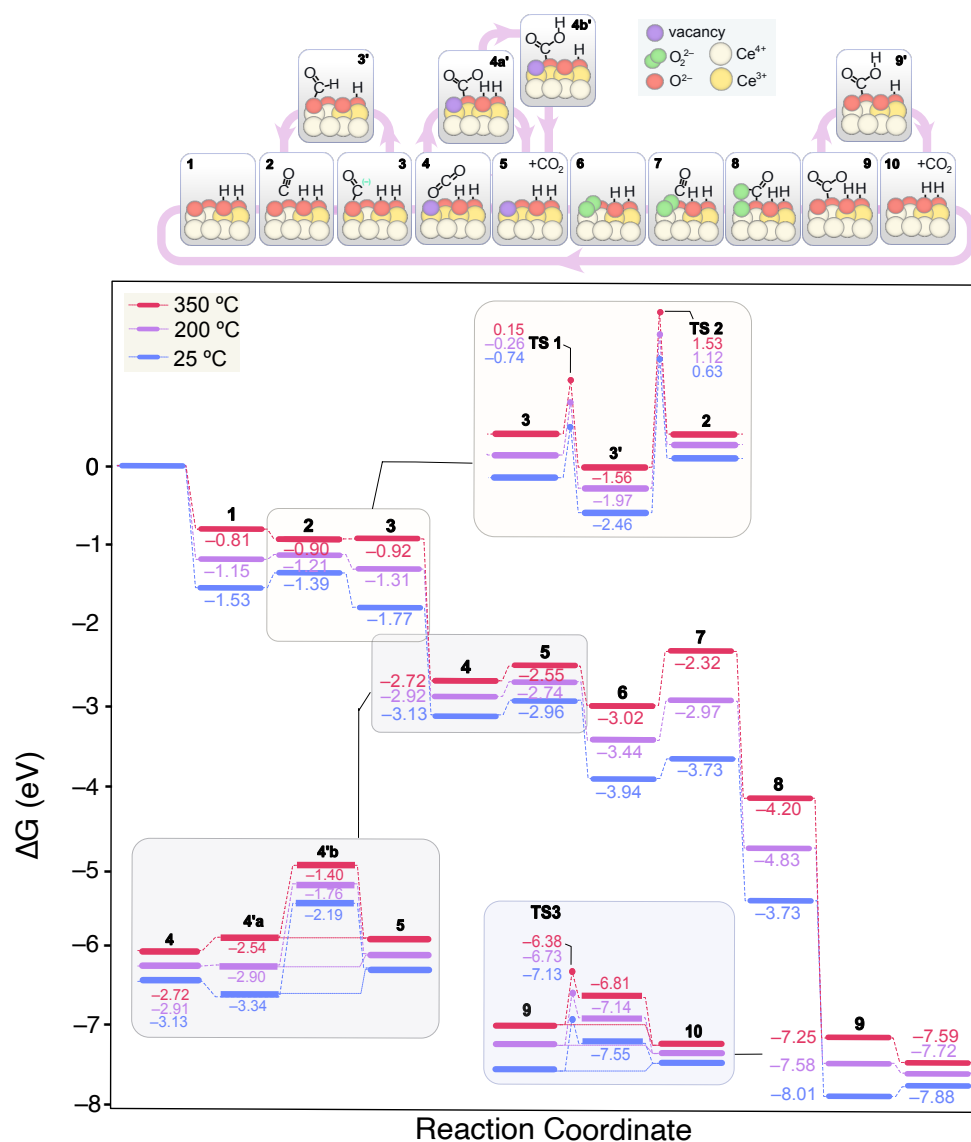
Figure 7. Calculated Gibbs energy diagram for the CO oxidation mechanism on a stoichiometric $CeO_2(111)$ surface covered with 2 OH groups at different experimental temperatures. The structures of the different reaction intermediates are depicted at the top of the diagram.

Calculations also predict that carboxylates do not form on the clean $CeO_2(111)$ surface, but they can be generated in the presence of a V^O and OH groups, which are typically found in real ceria surfaces. Since formates evolution is hindered and independent of the OH coverage during CO oxidation, we conclude that these species are mere spectators. Alternatively, carboxylates can evolve as CO_2, leaving behind a surface V^O (**4**). The generated CO_2 can then be readsorbed on a O^{2-} site to give rise to a carbonate (**4a'**), a process that is exergonic by ca. 0.2 eV at room temperature. In contrast to the clean surface, carbonate formation competes with CO_2 desorption (**5**). However, since OH groups tend to stabilize carbonates on the surface (see Table S1), the presence of a new OH group is expected to favor the presence of carbonates over CO_2 desorption. This situation is reversed at 200 °C and higher temperatures, and CO_2 desorption prevails regardless of the coverage. While on the surface, carbonates can also be hydrogenated to bicarbonates via H transfer from the coverage (**4b'**), which are less stable. As previously discussed by some of us and others [30,31], a higher bicarbonates-to-carbonates ratio enhances the CO-PROX activity in CuO/CeO_2 catalysts. Furthermore, the depletion of the hydroxyl band correlates with the bicarbonate formation rate. However, according to our DFT calculations, this

process has associated a TS with an energy barrier of 0.87 eV (TS3) at room temperature, and therefore, is likely to be able to compete with CO_2 desorption. When comparing the calculated barriers at higher OH coverages, we observe that bicarbonate formation is slightly facilitated (i.e., 0.79 vs. 0.87 eV, see Figure S6). Altogether, the bicarbonate route does not seem to be feasible on the (111) surface based on the calculated reaction thermodynamics and kinetics. In fact, this would not be a limiting step in metal-free ceria catalysts since much higher temperatures are needed to overcome the CO oxidation onset. However, as depicted by the energies of CO_x + OH adsorbates (Tables S1–S3), the (100) surface is the most prone to accumulate carbonates as these species are remarkably stabilized. Hence, in this minor facet, we envision that bicarbonates may have a key role in the CO-PROX catalysis at low temperatures.

Regardless of the reaction pathway, CO_x is released as CO_2 to the gas phase, followed by the regeneration of the V^O by a gas O_2 molecule **(6)**. To shed light into this process, we investigated all the possible reaction pathways. Firstly, we considered an additional CO adsorbed on a surface still containing the carbonate and the V^O, while leaving the O_2 uptake to the end of the CO oxidation cycles. This reaction pathway was found to be higher in energy all along the reaction cycle since O_2 stabilizes the reaction intermediates. Secondly, we explored the V^O restoration by O_2 whilst maintaining on surface the carbonate, which is a dead-end unless the carbonate releases the active site since CO(g) and O_2^{2-} do not interact in these conditions. Thus, the mechanism proposed in Figure 7 is the lowest energy pathway encountered. The second CO molecule finds a free O^{2-} site after CO_2 desorption. Instead of forming a carboxylate, we found that a O–O–COO intermediate is stabilized as a result of the $CO-O_2^{2-}$ interaction **(8)**. This intermediate has an elongated O–O bond at 1.497 Å, indicative of the O_2^{2-} dissociation degree, while the C–O bond distance is 1.436 Å and the lattice O is displaced upwards from its ground position. Subsequently, this structure leads to a bidentate carbonate and a surface oxygen **(9)** via the rearrangement of the surface and the O–O bond cleavage. The desorption of the resulting carbonate regenerates the initial state of the catalyst.

- CeO_2(110) surface

Unlike the (111) surface, CO adsorption on the (110) facet leads to highly stable bidentate carbonates in presence or absence of OH groups. Importantly, CO adsorption involves the reduction of two surface Ce^{4+} cations and the oxidation of C. Nevertheless, for catalytic CO oxidation, the product must be desorbed and the active site regenerated. The carbonates desorption to CO_2 involves an up-hill process of 2.32 eV, whereas their protonation to less stable bicarbonates goes through a high energy TS of 3.7 eV (see Figure S7). On the (110) surface, two types of bicarbonates can be formed, labeled herein as type A and B. The former are bound in a bidentate fashion and are more stable than the B-type by ca. −0.3 eV (see Figure 5b). The formation of type B bicarbonates from carbonates is more hampered due to the lower accessibility of the O being protonated. However, the evolution of type A bicarbonates to CO_2 + OH involves more rearrangement and thus higher energies due to the greater distance of H^+ to the surface. Hence, we propose that type A bicarbonates evolve to the B type through a low energy (i.e., 1.25 eV) H migration, from which CO_2 can be released more easily (Figure S8). These insights are depicted in Figure 8, which displays the obtained lower energy CO oxidation mechanism computed for the 3 OH-covered surface. Figure S9 depicts the analogue mechanism for the 6-OH coverage and the adsorbates energies are displayed in Table S2. As in the case of CeO_2(111), with the OH coverage, the lesser the barrier energies for the overall CO oxidation process, though this cannot be attributed to the more facile bicarbonates formation.
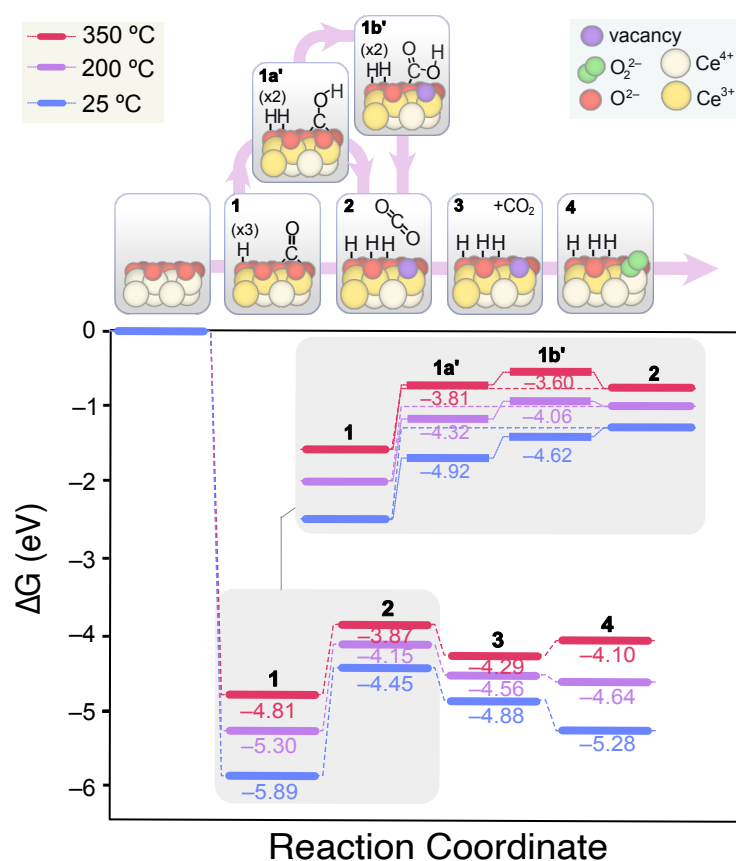
Figure 8. Calculated Gibbs energy diagram for the CO oxidation mechanism on a stoichiometric $CeO_2(110)$ surface covered with 3 OH groups at different experimental temperatures. The structures of the different reaction intermediates are depicted at the top of the diagram.

- $CeO_2(100)$ surface

Despite being the least stable surface, the (100) facet might also contribute to the CO oxidation process in polycrystalline ceria catalysts. According to our calculations, CO adsorption on (100) is weak, as in the case of (111), and CO oxidation proceeds via a similar reaction mechanism. However, the (100) surface is less dense, and its more open structure is able to stabilize multidentate carbonates whose desorption is strongly hampered. Thus, the (100) surface may reabsorb and retain the released CO_2 either through this or other catalytically active surfaces, increasing the accumulation of product-type adsorbates and leading to surface poisoning. In this case, the protonation of multidentate carbonates to bidentate bicarbonates is pivotal to boost CO_2 release, a process that is computed to be endergonic by ca. 1.90 eV (see Table S3). Given that this energy input is important, the greater abundance of the (100) facet on ceria crystals can be tentatively related to a poorer overall CO oxidation activity.

3. Discussion

The low-index CeO_2 surfaces display different features that have a momentous impact on their catalytic behavior, and the observed performance in realistic catalysts is an average of the actuation of the facets present. We can confirm that for CO oxidation, the (110) termination is the most favorable due to a facile V^O formation owing to its open structure. According to DRIFTS, the surface chemistry of the catalyst is under more dynamic adsorption-desorption equilibria with H_2 presence.

Interestingly, the adsorbates formed alongside the reaction cycle and their relative trends do not depend on H_2 feeding neither the CO oxidation onset varies significantly. This has been rationalized in detail for each of the surfaces.

On a theoretically clean and stoichiometric ceria (111) surface, CO will be weakly physisorbed. The reaction between CO and adsorbed $^*O_2$ was not observed to occur in the DFT simulations. In contrast, when sufficient energy is provided, the reaction between CO and surface O can take place, resulting in $CO_2 + V^O$ via an Eley–Rideal-like mechanism. The generated CO_2 could be readsorbed on the surface as a carbonate on a neighboring O surface site, although our computed energies indicate that this process is less favored compared to the direct release of CO_2 into the gas phase. The high reaction onset experimentally seen for CO oxidation on metal-free ceria catalysts cannot however be explained by this mechanism since none of the reaction steps are very energy demanding. However, this proposed mechanism is more ideal since CO-TOX operando DRIFTS revealed the presence of H-based species such as formates, suggesting the participation of highly stable intrinsic OH groups in the real catalyst operation.

In presence of H_2, the (111) surface is fully covered by OH groups which hinder CO adsorption. Thus, CO chemisorbs when O surface sites are available upon OH re-combination and H_2O release in the reaction conditions, leading to carboxylates (CO_2^{-d}). These species are formed solely when the surface is reduced either by the presence of V^O or OH groups, and their evolution can give rise to stable formates, which we find to act as spectators. Alternatively, carboxylates may be released as CO_2 while creating a V^O to be replenished by molecular oxygen. Although CO adsorption is hampered due to the lack of O surface sites, the redox features of the hydroxylated surface benefit the CO-ceria interaction, and therefore, promote the Mars–van Krevelen mechanism. We infer that the high reaction onset observed experimentally in CO-PROX may be due to the low concentration of available O sites due to the high level of hydroxylation of the surface, as the OH groups are less basic and are unable to react with CO.

Compared to the clean surface, when hydroxyl groups cover the (111) surface, carbonates become more stable. However, at temperatures around the CO oxidation onset, those species will be released as CO_2 gas. The possibility of OH groups forming the less stable bicarbonates via H transfer to adsorbed carbonates has been ruled out, especially at given the high temperatures required to initiate the reaction with metal-free ceria.

The reaction mechanism assessed for the (110) surface terminated with3 OH groups indicates that this surface displays a better catalytic performance, in agreement with multiple precedent experimental studies. CO binds with two surface O to give rise to carbonates while reducing two neighboring Ce^{4+} cations in a highly exergonic and straightforward CO oxidation. This process occurs at room temperature, as evidenced by the carbonate bands early appearance in DRIFTS. However, the remarkable stability of carbonates prevents the progress of the CO oxidation reaction. Experimentally, despite the early confirmation of carbonates, the CO oxidation onset was determined above ca. 250 °C with little positive effect of H_2 in the reactant mixture. Carbonates' hydrogenation on (110) facilitates the desorption of CO_x intermediates but implies higher activation energies than the release of the carbonates, and therefore, this route is not favored. Finally, the (100) surface is inferred to have the poorest catalytic performance given its weak CO adsorption and the strong binding of multidentate carbonates, which fall in a thermodynamic sink. The active site release is therefore impeded by strongly bounded products. In this surface, the formation of less stable bicarbonates (by ca. +2 eV), resulting from the proton transfer of neighboring OHs to carbonates is deemed to have a key role in CO oxidation.

In conclusion, we have presented a combined experimental/theoretical study of the CO-PROX process on metal-free ceria surfaces in presence and absence of hydrogen to examine the effect of H_2. Our results reveal that hydrogen improves the interaction between CO and ceria, although the reaction onset is not lowered compared to the H_2-free environment due to the lack of available O surface sites, which become hydroxylated in the presence of H_2. We have also shown that the carbonate to bicarbonate route is feasible on the (110) and (100) surfaces, but not on the main (111) facet, and only provided the reaction occurs at low temperatures. However, this route could have a significant role in metal-supported ceria catalysts, where the reaction onsets can be close to room

temperature. Herein we have evaluated the full reaction path considering a pure ceria surface with difficulties to bind CO. In metal-supported ceria catalysts, on the contrary, metals display high CO oxidation activity, and the released CO_2 is captured by a defect-rich ceria surface at low temperatures. It is in these conditions where the bicarbonates route may have a key role on the (110) and (100) facets to prevent the poisoning of the surface due to the accumulation of CO_x species.

4. Materials and Methods

4.1. Synthesis of Nano-Shaped Ceria Samples

Polycrystalline CeO_2 was obtained by direct calcination of the salt precursor $(Ce(NO_3)_3 \cdot 6H_2O$, Alfa Aesar 99.5%) in a muffle furnace at 500 °C for 2 h under a heating pace of 10 °C/min. CeO_2 cubes and CeO_2 rods were synthesized by adapting reported hydrothermal methodologies [81,82]. Namely, 4.0 mmol of $Ce(NO_3)_3 \cdot 6H_2O$ (Alfa Aesar, Haverhill, MA, USA) and 0.48 mmol of NaOH (pellets, Fisher Chemical, Hampton, NH, USA) were mixed in an aqueous solution of 80 mL of total volume and stirred for 30 min at room temperature. The resulting slurries were transferred to Teflon vessels and placed inside stainless-steel autoclaves. The sealed autoclaves were heated for 24 h in an electric oven with high precision temperature regulation. In the case of cubes, the temperature was set to 180 °C, while for rods, the temperature only reached 100 °C. After the thermal process, and once the autoclaves were cooled-down, the mixtures were centrifuged, and the isolated products were pH-neutralized by washing with distilled water and ethanol. The solids were kept at 80 °C for 12 h and then calcined at 500 °C following the same heating protocol as in the polycrystalline ceria.

4.2. Physicochemical Characterization of the Materials

The textural features of the nano-shaped ceria materials were assessed by N_2 physisorption at −196 °C (Autosorb-6, Quantachrome, Boynton Beach, FL, USA). Prior to the adsorption-desorption processes, samples were outgassed at 150 °C for 4 h. Raman spectroscopy analysis were conducted using He:Ne laser as light source (633 nm) in a NRS-5100 dispersive Raman instrument (Jasco, Tokyo, Japan) equipped with a four-stage Peltier cooled CCD detector. TEM was performed using a JEM-2010 (Jeol, Tokyo, Japan) microscope. The crystalline features of the prepared materials were studied by means of XRD performed with a Bruker D8-Advance diffractometer operating with Cu K radiation. The diffractograms were recorded at steps of 0.05° with 3 s per step. XPS analysis was performed under ultra-high vacuum with an Al Kα (1486.6 eV) X-ray source using a K-Alpha spectrophotometer (Thermo- Scientific, Waltham, MA, USA).

4.3. CO oxidation Operando DRIFTS Experiments

DRIFT spectra were recorded in a FT/IR-4000 infrared spectrometer (Jasco) at the time CO oxidation (CO-TOX and CO-PROX) was monitored at different reaction stages. To do so, 100 mg of the ceria catalyst was placed in a Praying Mantis high temperature reaction chamber (Harrick Scientific, Pleasantville, NY, USA) with gas flow regulated by mass flow controllers (Bronkhorst, Ruurlo, The Netherlands). The outlet gases were tracked using a OmniStar GSD 301 mass spectrometer (Pfeiffer Vacuum, Asslar, Germany) to assess the advance of the reaction. In CO-TOX experiments, the gas reactant mixture was composed of 2% O_2, 2% CO balanced with He up to a total flow of 50 mL/min. On the other hand, in CO-PROX catalytic tests, the gas mixture fed into the reaction cell consisted of 2% O_2, 2% CO and a 30% of H_2 with He balance (50 mL/min). Spectra were recorded once steady state conditions were reached at the different temperatures, increased at variable steps (25 or 50 °C) from 30 to 400 °C. Prior to measurements, the catalyst was pretreated (oxidized) in situ at 250 °C for 1h in a 20 mL/min flow of 10% O_2/He. After cooling down to 30 °C, the atmosphere was switched to He flow and the background spectrum was recorded in these conditions, before feeding the reaction gas mixtures.

4.4. DFT Calculations

DFT calculations were performed with the Vienna ab-initio simulation package (VASP) code (version 5.4.4) [83] implementing the Perdew–Burke–Ernzenhof (PBE) exchange correlation functional [84]. The core electrons of Ce, O, C and H ions were described with projector augmented wave (PAW) potentials [85], while their valence electrons were treated with plane-waves with a kinetic cut-off energy of 500 eV. An on-site correction for the localized 4f electrons of Ce was applied using an effective Hubbard U term (U_{eff}) of 4.5 eV following Dudarev's approach [86].

The fluorite bulk CeO_2 structure was optimized with a Γ-centered Monkhorst–Pack k-point grid of $7 \times 7 \times 7$, and the optimum lattice parameter was assessed using the Birch–Murnaghan equation of state. The optimized bulk structure was cleaved along the corresponding planes to build the (1 1 1), (1 0 0) and (1 1 0) surface slabs, representative of the most exposed ceria facets. A vacuum gap perpendicular to the surface of at least 15 Å was added to the surface models to avoid interaction between slabs along the z-axis. All surface slabs were optimized using a k-point mesh of $3 \times 3 \times 1$, and the computed adsorption energies, ΔE_{ads}, were calculated as:

$$\Delta E_{ads} = E_{ads+slab} - (E_{slab} + E_{ads}) \tag{1}$$

where E_{slab} is the energy of the clean slab, E_{ads} is the energy of the adsorbate species in the gas phase, and $E_{ads+slab}$ is the energy of the slab with the adsorbate in the most favorable configuration. Gibbs energy corrections where calculated to obtain the corresponding Gibbs adsorption energies and to investigate the effect of the reaction temperature using the following equation:

$$\Delta G_{ads}(T,p_0) = \Delta E_{ads} + \Delta E_{ZPE} - T\Delta S_{ads} \tag{2}$$

where ΔE_{ZPE} and $T\Delta S_{ads}$ denote the changes in zero-point energies and entropy, respectively, relative to the clean slab and the adsorbate molecules in the gas phase. The effect of H_2, CO and O_2 partial pressures on the calculated Gibbs adsorption energies was introduced as follows:

$$\Delta G_{ads}(T,p) = [\Delta G_{ads}(T,p_0) - \Sigma n \cdot \Delta \mu_i(T,p)] \tag{3}$$

where $\Delta \mu i(T,p)$ is the change in chemical potential of the n adsorbed species i at a given temperature and pressure, defined as:

$$\Delta \mu_i(T,p) = \Delta \mu_i(T,p_0) + \alpha \cdot k_B T \, ln(p_i/p_0) \tag{4}$$

where k_B is the Boltzmann constant, α is taken as $\frac{1}{2}$ for H_2 and 1 for CO, and $\Delta \mu_i(T,p_0)$ is the change in chemical potential for H_2 or CO at a given temperature and standard pressure.

Transition states (TS) for the relevant steps were located by means of the climbing image nudge elastic band method (CI-NEB) using at least f images along the reaction coordinate and the limited-memory Broyden–Fletcher–Goldfarb–Shanno (LBFGS) optimizer. The nature of TSs obtained was verified via vibrational frequency analysis using the finite difference method with a displacement of 0.01 Å.

References

1. Dey, S.; Dhal, G.C. Cerium catalysts applications in carbon monoxide oxidations. *Mater. Sci. Energy Technol.* **2020**, *3*, 6–24. [CrossRef]
2. Rodriguez, J.A.; Grinter, D.C.; Liu, Z.; Palomino, R.M.; Senanayake, S.D. Ceria-based model catalysts: Fundamental studies on the importance of the metal–ceria interface in CO oxidation, the water–gas shift, CO_2 hydrogenation, and methane and alcohol reforming. *Chem. Soc. Rev.* **2017**, *46*, 1824–1841. [CrossRef]
3. Beckers, J.; Rothenberg, G. Sustainable selective oxidations using ceria-based materials. *Green Chem.* **2010**, *12*, 939–948. [CrossRef]
4. Başar, M.S.; Çağlayan, B.S.; Aksoylu, A.E. A study on catalytic hydrogen production: Thermodynamic and experimental analysis of serial OSR-PROX system. *Fuel Process. Technol.* **2018**, *178*, 301–311. [CrossRef]
5. Poggio-Fraccari, E.; Abele, A.; Zitta, N.; Francesconi, J.; Mariño, F. CO removal for hydrogen purification via Water Gas Shift and COPROX reactions with monolithic catalysts. *Fuel* **2021**, 122419, in press. [CrossRef]
6. Farrauto, R.; Hwang, S.; Shore, L.; Ruettinger, W.; Lampert, J.; Giroux, T.; Liu, Y.; Ilinich, O. Generating Hydrogen for the PEM Fuel Cell. *Annu. Rev. Mater. Res.* **2003**, *33*, 1–27. [CrossRef]
7. Shabani, B.; Hafttananian, M.; Khamani, S.; Ramiar, A.; Ranjbar, A.A. Poisoning of proton exchange membrane fuel cells by contaminants and impurities: Review of mechanisms, effects, and mitigation strategies. *J. Power Source* **2019**, *427*, 21–48. [CrossRef]
8. Molochas, C.; Tsiakaras, P. Carbon Monoxide Tolerant Pt-Based Electrocatalysts for H_2-PEMFC Applications: Current Progress and Challenges. *Catalysts* **2021**, *11*, 1127. [CrossRef]
9. Yoshida, Y.; Izumi, Y. Recent Advances in the Preferential Thermal-/Photo-Oxidation of Carbon Monoxide: Noble Versus Inexpensive Metals and Their Reaction Mechanisms. *Catal. Surv. Asia* **2016**, *20*, 141–166. [CrossRef]
10. Gamarra, D.; Cámara, A.L.; Monte, M.; Rasmussen, S.B.; Chinchilla, L.E.; Hungría, A.B.; Munuera, G.; Gyorffy, N.; Schay, Z.; Corberán, V.C.; et al. Preferential oxidation of CO in excess H_2 over CuO/CeO_2 catalysts: Characterization and performance as a function of the exposed face present in the CeO_2 support. *Appl. Catal. B Environ.* **2013**, *130–131*, 224–238. [CrossRef]
11. Polster, C.S.; Nair, H.; Baertsch, C.D. Study of active sites and mechanism responsible for highly selective CO oxidation in H_2 rich atmospheres on a mixed Cu and Ce oxide catalyst. *J. Catal.* **2009**, *266*, 308–319. [CrossRef]
12. Zhang, R.; Miller, J.T.; Baertsch, C.D. Identifying the active redox oxygen sites in a mixed Cu and Ce oxide catalyst by in situ X-ray absorption spectroscopy and anaerobic reactions with CO in concentrated H_2. *J. Catal.* **2012**, *294*, 69–78. [CrossRef]
13. Martínez-Arias, A.; Gamarra, D.; Fernández-García, M.; Hornés, A.; Belver, C. Spectroscopic Study on the Nature of Active Entities in Copper–Ceria CO-PROX Catalysts. *Top. Catal.* **2009**, *52*, 1425–1432. [CrossRef]
14. Wang, L.; Deo, S.; Dooley, K.; Janik, M.J.; Rioux, R.M. Influence of metal nuclearity and physicochemical properties of ceria on the oxidation of carbon monoxide. *Chin. J. Catal.* **2020**, *41*, 951–962. [CrossRef]
15. Konsolakis, M.; Lykaki, M. Recent Advances on the Rational Design of Non-Precious Metal Oxide Catalysts Exemplified by CuO_x/CeO_2 Binary System: Implications of Size, Shape and Electronic Effects on Intrinsic Reactivity and Metal-Support Interactions. *Catalysts* **2020**, *10*, 160. [CrossRef]
16. Qiu, Z.; Guo, X.; Mao, J.; Zhou, R. New Design and Construction of Abundant Active Surface Interfacial Copper Entities in $Cu_xCe_{1−x}O_2$ Nanorod Catalysts for CO-PROX. *J. Phys. Chem. C* **2021**, *125*, 9178–9189. [CrossRef]
17. Castaldi, M.J. Removal of Trace Contaminants from Fuel Processing Reformate: Preferential Oxidation (Prox). In *Hydrogen and Syngas Production and Purification Technologies*; Liu, K., Song, C., Subramani, V., Eds.; John Wiley & Sons: Hoboken, NJ, USA, 2009; pp. 329–356.

18.   Zhang, R.; Haddadin, T.; Rubiano, D.P.; Nair, H.; Polster, C.S.; Baertsch, C.D. Quantification of Reactive CO and H_2 on CuO_x-CeO_2 during CO Preferential Oxidation by Reactive Titration and Steady State Isotopic Transient Kinetic Analysis. *ACS Catal.* **2011**, *1*, 519–525. [CrossRef]

19.   Martínez-Arias, A.; Hungría, A.B.; Munuera, G.; Gamarra, D. Preferential oxidation of CO in rich H_2 over CuO/CeO2: Details of selectivity and deactivation under the reactant stream. *Appl. Catal. B Environ.* **2006**, *65*, 207–216. [CrossRef]

20.   Sedmak, G.; Hočevar, S.; Levec, J. Kinetics of selective CO oxidation in excess of H_2 over the nanostructured $Cu_{0.1}Ce_{0.9}O_{2-y}$ catalyst. *J. Catal.* **2003**, *213*, 135–150. [CrossRef]

21.   Polster, C.S.; Baertsch, C.D. Application of CuO_x–CeO_2catalysts as selective sensor substrates for detection of CO in H_2 fuel. *Chem. Commun.* **2008**, *34*, 4046–4048. [CrossRef] [PubMed]

22.   Chen, J.; Yan, L.; Song, W.; Xu, D. Kinetic interplay between hydrogen and carbon monoxide in syngas-fueled catalytic micro-combustors. *Int. J. Hydrogen Energy* **2017**, *42*, 12681–12695. [CrossRef]

23.   Snytnikov, P.V.; Popova, M.M.; Men, Y.; Rebrov, E.V.; Kolb, G.; Hessel, V.; Schouten, J.C.; Sobyanin, V.A. Preferential CO oxidation over a copper–cerium oxide catalyst in a microchannel reactor. *Appl. Catal. A Gen.* **2008**, *350*, 53–62. [CrossRef]

24.   Lee, H.C.; Kim, D.H. Kinetics of CO and H_2 oxidation over CuO-CeO_2 catalyst in H_2 mixtures with CO_2 and H_2O. *Catal. Today* **2008**, *132*, 109–116. [CrossRef]

25.   Ayastuy, J.L.; Gurbani, A.; González-Marcos, M.P.; Gutiérrez-Ortiz, M.A. Kinetics of Carbon Monoxide Oxidation over CuO Supported on Nanosized CeO_2. *Ind. Eng. Chem. Res.* **2009**, *48*, 5633–5641. [CrossRef]

26.   Zou, H.; Chen, S.; Liu, Z.; Lin, W. DRIFTS study of Cu–Zr–Ce–O catalysts for selective CO oxidation. *Int. J. Hydrogen Energy* **2009**, *34*, 9324–9333. [CrossRef]

27.   Maeda, N.; Meemken, F.; Baiker, A. Insight into the mechanism of the preferential oxidation of carbon monoxide by using isotope-modulated excitation IR spectroscopy. *ChemCatChem* **2013**, *5*, 2199–2202. [CrossRef]

28.   Jacobs, G.; Williams, L.; Graham, U.; Thomas, G.A.; Sparks, D.E.; Davis, B.H. Low temperature water–gas shift: In situ DRIFTS-reaction study of ceria surface area on the evolution of formates on Pt/CeO_2 fuel processing catalysts for fuel cell applications. *Appl. Catal. A Gen.* **2003**, *252*, 107–118. [CrossRef]

29.   Denkwitz, Y.; Karpenko, A.; Plzak, V.; Leppelt, R.; Schumacher, B.; Behm, R.J. Influence of CO_2 and H_2 on the low-temperature water–gas shift reaction on Au/CeO_2 catalysts in idealized and realistic reformate. *J. Catal.* **2007**, *246*, 74–90. [CrossRef]

30.   Davó-Quiñonero, A.; Navlani-García, M.; Lozano-Castelló, D.; Bueno-López, A.; Anderson, J.A. Role of Hydroxyl Groups in the Preferential Oxidation of CO over Copper Oxide-Cerium Oxide Catalysts. *ACS Catal.* **2016**, *6*, 1723–1731. [CrossRef]

31.   Di Benedetto, A.; Landi, G.; Lisi, L. CO reactive adsorption at low temperature over CuO/CeO_2 structured catalytic monolith. *Int. J. Hydrogen Energy* **2017**, *42*, 12262–12275. [CrossRef]

32.   Hornés, A.; Bera, P.; Cámara, A.L.; Gamarra, D.; Munuera, G.; Martínez-Arias, A. CO-TPR-DRIFTS-MS in situ study of CuO/$Ce_{1-x}Tb_xO_{2-y}$ (x=0, 0.2 and 0.5) catalysts: Support effects on redox properties and CO oxidation catalysis. *J. Catal.* **2009**, *268*, 367–375. [CrossRef]

33.   Caputo, T.; Lisi, L.; Pirone, R.; Russo, G. On the role of redox properties of CuO/CeO_2 catalysts in the preferential oxidation of CO in H_2-rich gases. *Appl. Catal. A Gen.* **2008**, *348*, 42–53. [CrossRef]

34.   Pushkarev, V.V.; Kovalchuk, V.I.; d'Itri, J.L. Probing Defect Sites on the CeO_2 Surface with Dioxygen. *J. Phys. Chem. B* **2004**, *108*, 5341–5348. [CrossRef]

35.   Guo, M.; Lu, J.; Wu, Y.; Wang, Y.; Luo, M. UV and Visible Raman Studies of Oxygen Vacancies in Rare-Earth-Doped Ceria. *Langmuir* **2011**, *27*, 3872–3877. [CrossRef] [PubMed]

36.   Weber, W.H.; Hass, K.C.; McBride, J.R. Raman study of CeO_2: Second-order scattering, lattice dynamics, and particle-size effects. *Phys. Rev. B. Condens. Matter* **1993**, *48*, 178–185. [CrossRef]

37.   Schilling, C.; Hofmann, A.; Hess, C.; Ganduglia-Pirovano, M.V. Raman Spectra of Polycrystalline CeO_2: A Density Functional Theory Study. *J. Phys. Chem. C* **2017**, *121*, 20834–20849. [CrossRef]

38.   Kainbayev, N.; Sriubas, M.; Virbukas, D.; Rutkuniene, Z.; Bockute, K.; Bolegenova, S.; Laukaitis, G. Raman study of nanocrystalline-doped ceria oxide thin films. *Coatings* **2020**, *10*, 432. [CrossRef]

39.   Bueno-Ferrer, C.; Parres-Esclapez, S.; Lozano-Castelló, D.; Bueno-López, A. Relationship between surface area and crystal size of pure and doped cerium oxides. *J. Rare Earths* **2010**, *28*, 647–653. [CrossRef]

40.   Wu, Z.; Li, M.; Howe, J.; Meyer, H.M.; Overbury, S.H. Probing Defect Sites on CeO_2 Nanocrystals with Well-Defined Surface Planes by Raman Spectroscopy and O_2 Adsorption. *Langmuir* **2010**, *26*, 16595–16606. [CrossRef]

41.   Lin, Y.; Wu, Z.; Wen, J.; Poeppelmeier, K.R.; Marks, L.D. Imaging the Atomic Surface Structures of CeO_2 Nanoparticles. *Nano Lett.* **2014**, *14*, 191–196. [CrossRef]

42.   Deshpande, S.; Patil, S.; Kuchibhatla, S.V.N.T.; Seal, S. Size dependency variation in lattice parameter and valency states in nanocrystalline cerium oxide. *Appl. Phys. Lett.* **2005**, *87*, 133113–133116. [CrossRef]

43.   Trovarelli, A.; Llorca, J. Ceria Catalysts at Nanoscale: How Do Crystal Shapes Shape Catalysis? *ACS Catal.* **2017**, *7*, 4716–4735. [CrossRef]

44.   Tong, X.; Luo, T.; Meng, X.; Wu, H.; Li, J.; Liu, X.; Ji, X.; Wang, J.; Chen, C.; Zhan, Z. Shape-Dependent Activity of Ceria for Hydrogen Electro-Oxidation in Reduced-Temperature Solid Oxide Fuel Cells. *Small* **2015**, *11*, 5581–5588. [CrossRef] [PubMed]

45.   Lowell, S.; Shields, J.E.; Thomas, M.A.; Thommes, M. Characterization of Porous Solids and Powders: Surface Area, Pore Size and Density. In *Particle Technology Series*; Springer: Berlin/Heidelberg, Germany, 2004; Volume 16, ISSN 1567-827X.

46.   Thommes, M.; Kaneko, K.; Neimark, A.V.; Olivier, J.P.; Rodriguez-Reinoso, F.; Rouquerol, J.; Sing, K.S.W. Physisorption of gases, with special reference to the evaluation of surface area and pore size distribution (IUPAC Technical Report). *Pure Appl. Chem.* **2015**, *87*, 1051–1069. [CrossRef]

47.   Liu, Z.; Li, X.; Mayyas, M.; Koshy, P.; Hart, J.N.; Sorrell, C.C. Growth mechanism of ceria nanorods by precipitation at room temperature and morphology-dependent photocatalytic performance. *CrystEngComm* **2017**, *19*, 4766–4776. [CrossRef]

48.   Nolan, M.; Grigoleit, S.; Sayle, D.C.; Parker, S.C.; Watson, G.W. Density functional theory studies of the structure and electronic structure of pure and defective low index surfaces of ceria. *Surf. Sci.* **2005**, *576*, 217–229. [CrossRef]

49.   Montini, T.; Melchionna, M.; Monai, M.; Fornasiero, P. Fundamentals and Catalytic Applications of CeO_2-Based Materials. *Chem. Rev.* **2016**, *116*, 5987–6041. [CrossRef] [PubMed]

50.   Doornkamp, C.; Ponec, V. The universal character of the Mars and Van Krevelen mechanism. *J. Mol. Catal. A Chem.* **2000**, *162*, 19–32. [CrossRef]

51.   Capdevila-Cortada, M.; Vilé, G.; Teschner, D.; Pérez-Ramírez, J.; López, N. Reactivity descriptors for ceria in catalysis. *Appl. Catal. B Environ.* **2016**, *197*, 299–312. [CrossRef]

52.   Zhou, M.; Cai, L.; Bajdich, M.; García-Melchor, M.; Li, H.; He, J.; Wilcox, J.; Wu, W.; Vojvodic, A.; Zheng, X. Enhancing Catalytic CO Oxidation over Co_3O_4 Nanowires by Substituting Co^{2+} with Cu^{2+}. *ACS Catal.* **2015**, *5*, 4485–4491. [CrossRef]

53.   Farra, R.; García-Melchor, M.; Eichelbaum, M.; Hashagen, M.; Frandsen, W.; Allan, J.; Girgsdies, F.; Szentmiklósi, L.; López, N.; Teschner, D. Promoted Ceria: A Structural, Catalytic, and Computational Study. *ACS Catal.* **2013**, *3*, 2256–2268. [CrossRef]

54.   Kropp, T.; Mavrikakis, M. Brønsted–Evans–Polanyi relation for CO oxidation on metal oxides following the Mars–van Krevelen mechanism. *J. Catal.* **2019**, *377*, 577–581. [CrossRef]

55.   Ganduglia-Pirovano, M.V.; Da Silva, J.L.F.; Sauer, J. Density-Functional Calculations of the Structure of Near-Surface Oxygen Vacancies and Electron Localization on CeO_2(111). *Phys. Rev. Lett.* **2009**, *102*, 26101–26105. [CrossRef]

56.   Zhao, Y.; Teng, B.-T.; Wen, X.-D.; Zhao, Y.; Chen, Q.-P.; Zhao, L.-H.; Luo, M.-F. Superoxide and Peroxide Species on CeO_2(111), and Their Oxidation Roles. *J. Phys. Chem. C* **2012**, *116*, 15986–15991. [CrossRef]

57.   Huang, M.; Fabris, S. Role of surface peroxo and superoxo species in the low-temperature oxygen buffering of ceria: Density functional theory calculations. *Phys. Rev. B* **2007**, *75*, 81404–81408. [CrossRef]

58.   Choi, Y.M.; Abernathy, H.; Chen, H.-T.; Lin, M.C.; Liu, M. Characterization of O_2–CeO_2 Interactions Using In Situ Raman Spectroscopy and First-Principle Calculations. *ChemPhysChem* **2006**, *7*, 1957–1963. [CrossRef]

59.   Nolan, M. Healing of oxygen vacancies on reduced surfaces of gold-doped ceria. *J. Chem. Phys.* **2009**, *130*, 144702–144711. [CrossRef]

60.   Ziemba, M.; Schilling, C.; Ganduglia-Pirovano, M.V.; Hess, C. Toward an Atomic-Level Understanding of Ceria-Based Catalysts: When Experiment and Theory Go Hand in Hand. *Acc. Chem. Res.* **2021**, *54*, 2884–2893. [CrossRef]

61.   Feng, G.; Han, W.; Wang, Z.; Li, F.; Xue, W. Highly Reducible Nanostructured CeO2 for CO Oxidation. *Catalysts* **2018**, *8*, 535. [CrossRef]

62.   González-Rovira, L.; Sánchez-Amaya, J.M.; López-Haro, M.; del Rio, E.; Hungría, A.B.; Midgley, P.; Calvino, J.J.; Bernal, S.; Botana, F.J. Single-Step Process To Prepare CeO_2 Nanotubes with Improved Catalytic Activity. *Nano Lett.* **2009**, *9*, 1395–1400. [CrossRef]

63.   Zhang, X.; Hou, F.; Yang, Y.; Wang, Y.; Liu, N.; Chen, D.; Yang, Y. A facile synthesis for cauliflower like CeO_2 catalysts from Ce-BTC precursor and their catalytic performance for CO oxidation. *Appl. Surf. Sci.* **2017**, *423*, 771–779. [CrossRef]

64.   Si, R.; Flytzani-Stephanopoulos, M. Shape and crystal-plane effects of nanoscale ceria on the activity of $Au-CeO_2$ catalysts for the water-gas shift reaction. *Angew. Chemie-Int. Ed.* **2008**, *47*, 2884–2887. [CrossRef]

65.   Hadjiivanov, K. *Chapter Two—Identification and Characterization of Surface Hydroxyl Groups by Infrared Spectroscopy*; Jentoft, F.C., Ed.; Academic Press: Cambridge, MA, USA, 2014; Volume 57, pp. 99–318. ISBN 0360-0564.

66.   Saw, E.T.; Oemar, U.; Ang, M.L.; Kus, H.; Kawi, S. High-temperature water gas shift reaction on $Ni-Cu/CeO_2$ catalysts: Effect of ceria nanocrystal size on carboxylate formation. *Catal. Sci. Technol.* **2016**, *6*, 5336–5349. [CrossRef]

67.   Li, Y.; Kottwitz, M.; Vincent, J.L.; Enright, M.J.; Liu, Z.; Zhang, L.; Huang, J.; Senanayake, S.D.; Yang, W.-C.D.; Crozier, P.A.; et al. Dynamic structure of active sites in ceria-supported Pt catalysts for the water gas shift reaction. *Nat. Commun.* **2021**, *12*, 914–923. [CrossRef]

68.   Chen, B.; Ma, Y.; Ding, L.; Xu, L.; Wu, Z.; Yuan, Q.; Huang, W. Reactivity of Hydroxyls and Water on a CeO_2(111) Thin Film Surface: The Role of Oxygen Vacancy. *J. Phys. Chem. C* **2013**, *117*, 5800–5810. [CrossRef]

69.   Kammert, J.; Moon, J.; Wu, Z. A review of the interactions between ceria and H_2 and the applications to selective hydrogenation of alkynes. *Chin. J. Catal.* **2020**, *41*, 901–914. [CrossRef]

70.   García-Melchor, M.; López, N. Homolytic Products from Heterolytic Paths in H_2 Dissociation on Metal Oxides: The Example of CeO_2. *J. Phys. Chem. C* **2014**, *118*, 10921–10926. [CrossRef]

71.   Fernández-Torre, D.; Carrasco, J.; Ganduglia-Pirovano, M.V.; Pérez, R. Hydrogen activation, diffusion, and clustering on CeO_2(111): A DFT+U study. *J. Chem. Phys.* **2014**, *141*, 14703–14712. [CrossRef]

72.   Yang, Z.; Woo, T.K.; Hermansson, K. Strong and weak adsorption of CO on CeO_2 surfaces from first principles calculations. *Chem. Phys. Lett.* **2004**, *396*, 384–392. [CrossRef]

73.   Nolan, M.; Watson, G.W. The Surface Dependence of CO Adsorption on Ceria. *J. Phys. Chem. B* **2006**, *110*, 16600–16606. [CrossRef]

74.   Mudiyanselage, K.; Kim, H.Y.; Senanayake, S.D.; Baber, A.E.; Liu, P.; Stacchiola, D. Probing adsorption sites for CO on ceria. *Phys. Chem. Chem. Phys.* **2013**, *15*, 15856–15862. [CrossRef] [PubMed]

75. Huang, M.; Fabris, S. CO Adsorption and Oxidation on Ceria Surfaces from DFT+U Calculations. *J. Phys. Chem. C* **2008**, *112*, 8643–8648. [CrossRef]
76. Wang, X.; Li, M.; Wu, Z. In situ spectroscopic insights into the redox and acid-base properties of ceria catalysts. *Chin. J. Catal.* **2021**, *42*, 2122–2140. [CrossRef]
77. Wu, Z.; Mann, A.K.P.; Li, M.; Overbury, S.H. Spectroscopic Investigation of Surface-Dependent Acid–Base Property of Ceria Nanoshapes. *J. Phys. Chem. C* **2015**, *119*, 7340–7350. [CrossRef]
78. Chen, F.; Liu, D.; Zhang, J.; Hu, P.; Gong, X.Q.; Lu, G. A DFT+U study of the lattice oxygen reactivity toward direct CO oxidation on the CeO_2(111) and (110) surfaces. *Phys. Chem. Chem. Phys.* **2012**, *14*, 16573–16580. [CrossRef] [PubMed]
79. Chen, S.; Cao, T.; Gao, Y.; Li, D.; Xiong, F.; Huang, W. Probing Surface Structures of CeO_2, TiO_2, and Cu_2O Nanocrystals with CO and CO_2 Chemisorption. *J. Phys. Chem. C* **2016**, *120*, 21472–21485. [CrossRef]
80. López-Rodríguez, S.; Davó-Quiñonero, A.; Bailón-García, E.; Lozano-Castelló, D.; Herrera, F.C.; Pellegrin, E.; Escudero, C.; García-Melchor, M.; Bueno-López, A. Elucidating the Role of the Metal Catalyst and Oxide Support in the Ru/CeO_2-Catalyzed CO_2 Methanation Mechanism. *J. Phys. Chem. C* **2021**, *125*, 25533–25544. [CrossRef]
81. Aneggi, E.; Wiater, D.; de Leitenburg, C.; Llorca, J.; Trovarelli, A. Shape-Dependent Activity of Ceria in Soot Combustion. *ACS Catal.* **2014**, *4*, 172–181. [CrossRef]
82. Mai, H.-X.; Sun, L.-D.; Zhang, Y.-W.; Si, R.; Feng, W.; Zhang, H.-P.; Liu, H.-C.; Yan, C.-H. Shape-Selective Synthesis and Oxygen Storage Behavior of Ceria Nanopolyhedra, Nanorods, and Nanocubes. *J. Phys. Chem. B* **2005**, *109*, 24380–24385. [CrossRef] [PubMed]
83. Kresse, G.; Furthmüller, J. Efficient iterative schemes for ab initio total-energy calculations using a plane-wave basis set. *Phys. Rev. B* **1996**, *54*, 11169–11186. [CrossRef]
84. Perdew, J.P.; Burke, K.; Ernzerhof, M. Generalized Gradient Approximation Made Simple. *Phys. Rev. Lett.* **1996**, *77*, 3865–3868. [CrossRef]
85. Blöchl, P.E. Projector augmented-wave method. *Phys. Rev. B* **1994**, *50*, 17953–17979. [CrossRef]
86. Dudarev, S.L.; Botton, G.A.; Savrasov, S.Y.; Humphreys, C.J.; Sutton, A.P. Electron-energy-loss spectra and the structural stability of nickel oxide: An LSDA+U study. *Phys. Rev. B* **1998**, *57*, 1505–1509. [CrossRef]